Deperturbation treatment of the $A\,^1\Sigma^+-b\,^3\Pi$ complex of NaRb and prospects for ultracold molecule formation in $X\,^1\Sigma^+(v=0;J=0)$

O. Docenko, M. Tamanis, and R. Ferber

Department of Physics and Institute of Atomic Physics and Spectroscopy, University of Latvia, 19 Rainis Boulevard,
Riga LV-1586, Latvia

E. A. Pazyuk, A. Zaitsevskii, and A. V. Stolyarov

Department of Chemistry, Moscow State University, GSP-2 Leninskie gory 1/3, Moscow 119992, Russia

A. Pashov

Department of Physics, Sofia University, 5 James Bourchier Boulevard, 1164 Sofia, Bulgaria

H. Knöckel and E. Tiemann

Institut für Quantenoptik, Gottfried Wilhelm Leibniz Universität Hannover, Welfengarten 1, 30167 Hannover, Germany

High resolution Fourier transform spectra (FTS) of laser induced fluorescence (LIF) of $C\,^1\Sigma^+;D\,^1\Pi$ $\rightarrow A\,^1\Sigma^+-b\,^3\Pi$ and $A\,^1\Sigma^+-b\,^3\Pi\rightarrow X\,^1\Sigma^+$ transitions in Na^{85}Rb and Na^{87}Rb were obtained. An analysis of the direct LIF spectra together with the rotational relaxation satellites provided highly accurate rovibronic term values for ($4\leq J\leq 163$) of the $A\,^1\Sigma^+-b\,^3\Pi$ complex, covering about 1950 mostly singlet levels $0\leq v_A\leq 49$ and a considerable number (>360) of the predominantly triplet $b\,^3\Pi_{0,1}$ sublevels. The direct deperturbation analysis of the singlet-triplet $A-b$ complex was performed by means of the inverted channel-coupling approach with Hund's coupling case **a** basis functions. The electronic matrix elements of the model 4×4 Hamiltonian were defined as piecewise analytical functions of the internuclear distance. Besides the Born-Oppenheimer potential energy curves of the mutually perturbed states and the off-diagonal spin-orbit (SO) $A-b$ coupling function, the SO splitting of the $b\,^3\Pi$ state was determined due to the pronounced electronic-rotation interaction between the $b\,^3\Pi_0$ and $b\,^3\Pi_1$ components observed for high J levels. Overall, 24 mass-invariant fitting parameters have been required to reproduce about 2300 experimental term values of both isotopomers with a standard deviation of 0.012 cm^{-1}, which is consistent with the uncertainty of the FTS experiment. An analytical mapping procedure based on a reduced variable representation of the radial coordinate was used to diminish the computational effort for the uniform finite-difference grid solution of the coupled-channel equations. The derived nonadiabatic $A-b$ wave functions were used to evaluate the $A\,^1\Sigma^+-b\,^3\Pi-D\,^1\Pi$, $a\,^3\Sigma^+$, $X\,^1\Sigma^+$ rovibronic transition probabilities. The relative intensity distributions predicted for the $D\rightarrow A-b$ and $A-b\rightarrow X$ LIF progressions agree with their experimental counterparts within the accuracy of the measurements. The calculated $A-b-a$, X transition probabilities were applied for simulation of the stimulated Raman $a\rightarrow A-b\rightarrow X$ processes, which can lead to efficient formation of ultracold NaRb molecules in the ground level $v_X=0$; $J_X=0$.

PACS number(s): 31.50.−x, 33.50.Dq, 33.70.Fd, 33.80.Ps

I. INTRODUCTION

Production of ultracold polar molecules (UPM) has attracted particular attention for many reasons. The main one is the possibility of their control and manipulation with external electric fields due to the large permanent electric dipole moments. Different phenomena are expected under ultracold conditions such as new features in phase diagrams of degenerate states [1] and anisotropic collisions caused by anisotropic dipole-dipole interaction [2]. The application of UPMs as a species for quantum computing [3] and for checking fundamental symmetries [4] are also considered.

As far as Na or Rb containing mixed alkali-metal diatomics are considered, cold collision, photoassociation, or Feshbach resonance experiments were performed in Na-Li [5], K-Rb [6–8], Na-Cs [9], Na-Rb [10–12], and Rb-Cs [13]. The first promising results for the formation of ultracold heteronuclear diatomic molecules refer mostly to translationally

cold ones, which are in highly excited rovibronic levels. However, the production of ultracold polar RbCs molecules by photoassociation in the lowest rovibrational levels of the ground state was recently demonstrated [13].

Further progress in converting ultracold heteronuclear alkali-metal diatomic molecules to their ground state $v''_X=0$; $J''_X=0$ level could be expected by exploiting stimulated Raman transitions via intermediate levels belonging to the strongly mixed singlet-triplet $A\,^1\Sigma^+-b\,^3\Pi$ complex as proposed by Stwalley [14]. In Fig. 1 the lowest electronic singlet and triplet potential energy curves of NaRb from *ab initio* calculations [15] are shown. Efficient vertical triplet-triplet absorption pumping transitions (PUMP) transitions from the left turning point of the initial $a\,^3\Sigma^+(N''_a=0)$ levels lying near the Na(3s)+Rb(5s) dissociation limit to the right turning point of the upper $b\,^3\Pi(v'_b;J'=1)$ levels should be expected due to favorable Franck-Condon factors (FCFs). The intermediate triplet b state is strongly mixed with the
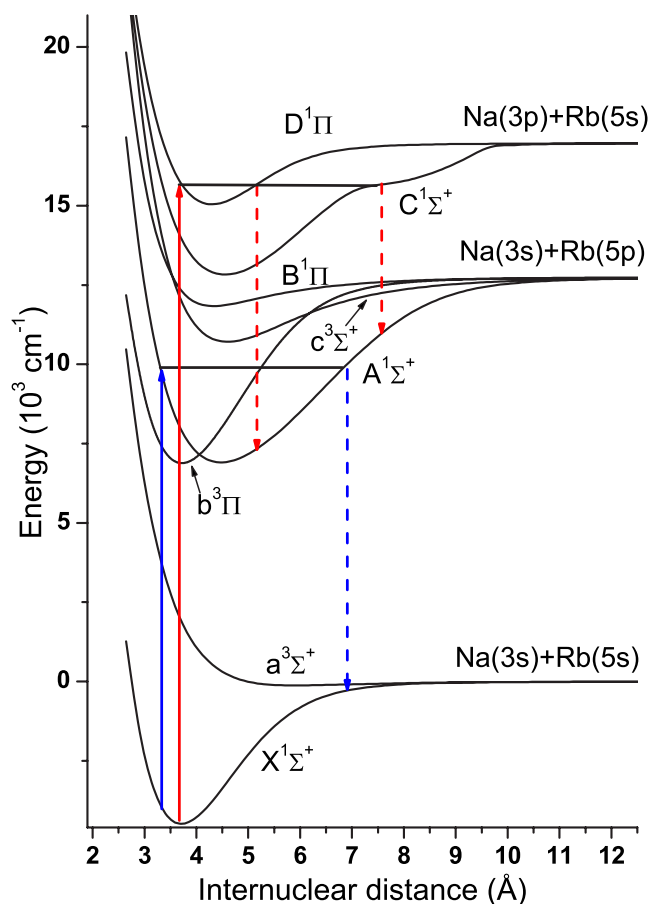
FIG. 1. (Color online) Schema of the lowest electronic states of the NaRb molecule [15] along with the laser excitation or FTS observation used in the present experiment.

nearest singlet $A\,{}^1\Sigma^+$ state due to the spin-orbit effect in the Rb(5p) atom. Therefore, rather efficient singlet-singlet stimulated emission transitions (DUMP) transitions from the left turning point of the $A\,{}^1\Sigma^+(v'_A, J'=1)$ levels to the ground $X\,{}^1\Sigma^+(v''_X=0; J''_X=0)$ level are possible in a stimulated Raman process. Furthermore, the maximal conversion rate to the lowest rovibronic level may be achieved by the time-dependent STIRAP scheme [16] when the proper inverse sequence of DUMP and PUMP pulses allows one to get an almost 100% efficiency for the $a\,{}^3\Sigma^+ \rightarrow A\,{}^1\Sigma^+ - b\,{}^3\Pi \rightarrow X\,{}^1\Sigma^+$ process under ultracold conditions. The rigorous exploration of the stimulated Raman processes apparently requires highly accurate nonadiabatic eigenvalues and eigenfunctions of the $A-b$ complex.

Reliable Born-Oppenheimer potential energy curves (BO PECs) for the $X\,{}^1\Sigma^+$, $a\,{}^3\Sigma^+$, $C\,{}^1\Sigma^+$, and $D\,{}^1\Pi$ states of NaRb have been recently obtained by high resolution Fourier transform spectroscopy (FTS) [17–20], while data of the same quality on the fully mixed $A\,{}^1\Sigma^+ - b\,{}^3\Pi$ complex are available in a very limited (v, J) region [21].

Ab initio spin-orbit-free BO PECs $U_i^{ab}(R)$, permanent $d_i^{ab}(R)$, and transition dipole moment $d_{ij}^{ab}(R)$ functions between the ground and low-lying excited states of the NaRb dimer have been obtained by calculations in the framework of the core-polarization potential (CPP) [15,22] and second order multipartitioning perturbation theory (MPPT) [21,23]. The spin-orbit (SO) coupling $\xi_{Ab}^{so}(R)$ of $A\,{}^1\Sigma^+ - b\,{}^3\Pi_0$ and the SO splitting $A_{b\,{}^3\Pi}^{so}(R)$ of the $b\,{}^3\Pi$ state were evaluated in the internuclear distance range $R \in [3,7]$ Å by means of the quasirelativistic pseudopotential calculation [21]. The nonrelativistic angular coupling matrix elements L_{ij}^{ab} among the lowest $(1-7)\,{}^1\Sigma^+$ and $B, D\,{}^1\Pi$ states are available in Ref. [23].

The first experimental studies of the singlet-triplet $A\,{}^1\Sigma^+ - b\,{}^3\Pi$ complex of the NaRb molecule [21] were performed by means of high resolution sub-Doppler laser spectroscopy applying a two-laser *V*-type pump-probe excitation scheme involving $X \rightarrow A - b$ transitions to the vibrational $A\,{}^1\Sigma^+(6 \leqslant v_A^* \leqslant 21)$ levels and low rotational quantum numbers $J \in [8,23]$. The experimental rovibronic term values of the complex were deperturbed by the inverted two-coupled-channels approach $(2\times2\ \text{ICCA-RKR})$ [24] based on a Rydberg-Klein-Rees (RKR) potential construction for both interacting states $A\,{}^1\Sigma^+$, $b\,{}^3\Pi_0$ and the explicit consideration of the SO $A\,{}^1\Sigma^+ - b\,{}^3\Pi_0$ coupling effect. The relative intensity distribution measured in Ref. [21] for long $A - b \rightarrow X$ LIF progressions in connection with the iterative ICCA procedure provided the correct vibrational identification of the levels involved. The resulting molecular parameters reproduce the very irregular pattern of the experimental rovibronic term values with a standard deviation of $0.3-0.5$ cm^{-1}, which is, however, far from the uncertainty of the measurements of 0.003 cm^{-1}. Later, in Ref. [25] the moderately accurate Hulburt-Hirschfelder potential has been constructed for the BO $A\,{}^1\Sigma^+$ state by means of the direct potential fit analysis of the experimental intensity distributions in the long $A - b \rightarrow X(v''_X \in [0,43])$ LIF series starting from the weakly perturbed levels of the $A - b$ complex.

In the present study FTS was applied to resolve infrared LIF transitions from the higher excited states $C\,{}^1\Sigma^+$, $D\,{}^1\Pi \rightarrow A\,{}^1\Sigma^+ - b\,{}^3\Pi$ as well as LIF to the ground state from the directly excited $A\,{}^1\Sigma^+ - b\,{}^3\Pi$ complex (see Fig. 1). The experimental data field has been extended considerably for both Na^{85}Rb and Na^{87}Rb isotopomers in comparison to the preceding work [21]. Indeed, about 2300 rovibronic term values with $4 \leqslant J \leqslant 163$ were obtained including vibrational levels $0 \leqslant v_A^* \leqslant 49$ of the singlet A state and a significant number of the predominantly triplet $b\,{}^3\Pi_0$ and even $b\,{}^3\Pi_1$ sublevels. A deperturbation analysis of this huge data set of experimental term values of the NaRb $A - b$ complex was performed by means of the inverted close-coupling approach (ICCA) [21,24,26], which is based on a numerical solution of the system of the coupled radial equations corresponding to the total nonadiabatic rovibronic molecular Hamiltonian [28] and the direct determination of the electronic parameters (i.e., potential energy curves and spin-orbit coupling matrix elements) in the framework of an iterative weighted nonlinear least-squares procedure. The ICCA method takes into account implicitly both strong local and weak regular intramolecular interactions caused by the overall set of mutually perturbed vibrational terms. Therefore, in contrast to the traditional effective Hamiltonian approach [27] the ICCA allows one to avoid completely the conventional truncation of the vibrational dimensionality of the inverse problem. How-

ever, the ICCA becomes a feasible procedure only when an initial set of electronic parameters approximated by the appropriate analytical functions is well defined over a wide range of internuclear distances, and its practical implementation inevitably requires a very efficient method for a numerical solution of the close-coupling radial equations. The direct deperturbation treatment of the $A\,^1\Sigma^+-b\,^3\Pi$ complex was performed by including explicitly the nondiagonal spin-orbit coupling and the electronic-rotational interaction [28,29] between the $\Omega=0,1,2$ components of the triplet $b\,^3\Pi$ state leading to wave functions of the intermediate **a**-**b**-**c** Hund's coupling case. The matrix elements of the model 4×4 Hamiltonian were defined as piecewise analytical functions of the internuclear distance. Such an approach improves efficiently the relevant nonlinear least-squared procedure based on calculations of the required Jacobian matrix with the Hellmann-Feynman theorem. An analytical mapping procedure with a reduced variable representation of the radial coordinate was used to diminish the computational effort of the uniformed finite-difference grid solution of the coupled-channels equations.

The paper is structured as follows. A brief description of the experiment as well as of the procedure of rovibrational assignment is given in Sec. II. The analytical model Hamiltonian and efficient mapping procedures used for direct deperturbation analysis of the complex are explained in Sec. III. The derived interatomic BO PECs and SO coupling functions are compared with the available experimental and theoretical results in Sec. IV. The wave numbers and probabilities of the PUMP-DUMP transitions for the stimulated Raman $a\rightarrow A-b\rightarrow X$ process are predicted in Sec. V.

II. FOURIER TRANSFORM SPECTROSCOPY OF THE $A-b$ COMPLEX

A. Experimental details

The NaRb $A\,^1\Sigma^+-b\,^3\Pi$ complex was studied experimentally by means of high resolution Fourier transform spectroscopy. Details of the experimental setup can be found in Ref. [17] and, hence, will be mentioned only briefly here. A gas sample of Na^{85}Rb and Na^{87}Rb isotopomers in natural composition is prepared in a stainless-steel heat pipe oven by heating a mixture of metallic Na ($\approx$10 g) and Rb ($\approx$5 g) up to 570 K. Argon at a pressure of 2–5 mbars was used as a buffer gas. Laser induced fluorescence (LIF) was resolved by a Bruker IFS 120 HR Fourier transform spectrometer with a typical resolution of 0.03 cm^{-1}, leading to line accuracies of 0.003 cm^{-1} for strong signals.

The 514.5, 496.5, 488.0, and 476.5 nm lines of a single-mode Ar$^+$ laser (Spectra Physics BeamLok 2060) were used to induce the infrared fluorescence $D\,^1\Pi\rightarrow A\,^1\Sigma^+-b\,^3\Pi$. In the case of the 514.5 nm line the $C\,^1\Sigma^+\rightarrow A\,^1\Sigma^+-b\,^3\Pi$ fluorescence also was observed (see Fig. 2). To simplify the assignment of the NaRb infrared spectra, the visible part of the $D\,^1\Pi,C\,^1\Sigma^+\rightarrow X\,^1\Sigma^+$ LIF spectra simultaneously excited with the same laser frequency were also recorded. The infrared spectra were detected with an In$_x$Ga$_{1-x}$As detector whereas for the visible region a photomultiplier was employed. The measured relative intensity distributions in the
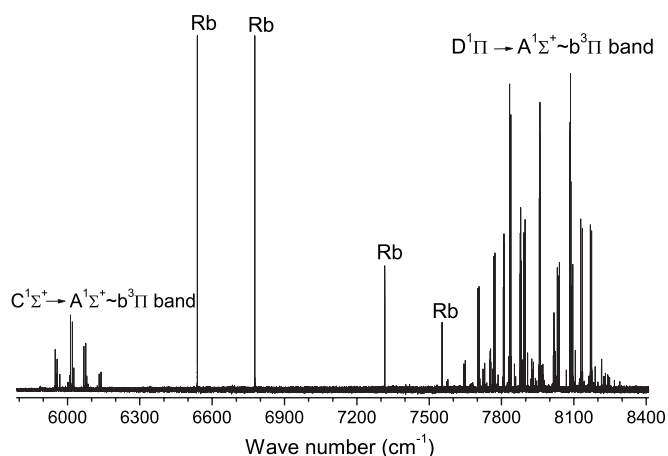

FIG. 2. Example of NaRb LIF infrared spectrum excited by the Ar$^+$ 514.5 nm line. Atomic Rb lines also can be seen in the spectrum.

infrared $D,C\rightarrow A-b$ LIF spectra were calibrated to account for the spectral sensitivity of the InGaAs detector.

For direct excitation of the $X\,^1\Sigma^+\rightarrow A\,^1\Sigma^+-b\,^3\Pi$ transitions (see, e.g., Fig. 3), a tunable single mode Ti:sapphire laser (typical power used is 150 mW) from Tekhnoscan, pumped by a frequency doubled Nd:YAG laser (Verdi, coherent radiation) was applied. The excitation range was 12 795–13 423 cm^{-1} and the corresponding $A\,^1\Sigma^+-b\,^3\Pi\rightarrow X\,^1\Sigma^+$ LIF spectra were detected with a Si diode.

B. Rovibrational assignment of the LIF spectra

The fully mixed character of the $A-b$ complex leads to strong irregularities in the vibrational and rotational spacings (see, e.g., Fig. 4). These irregularities made an unambiguous rotational assignment of the infrared $D\,^1\Pi,C\,^1\Sigma^+\rightarrow A\,^1\Sigma^+-b\,^3\Pi$ spectra almost impossible without the preceding rovibrational identification of the upper states. In order to get a list of the upper rovibronic levels the visible $D\,^1\Pi,C\,^1\Sigma^+\rightarrow X\,^1\Sigma^+$ spectra were recorded with the laser frequency tuned for obtaining maximum intensity for one selected $D,C\rightarrow X$ progression. Then, the corresponding infrared $D\,^1\Pi,C\,^1\Sigma^+\rightarrow A\,^1\Sigma^+-b\,^3\Pi$ spectrum was recorded. An assignment of the visible spectra was straightforward thanks to the previous FTS measurements and the accurate ground state PECs [17,20]. Identification of infrared progressions was also facilitated by the $A\,^1\Sigma^+$ state molecular constants from Ref. [21]. It should be noticed, however, that the vibrational assignment of the multichannel states is always an ambiguous procedure since the proposed vibrational quantum numbers v_A^*, v_b^* of the mutually perturbed states are not exactly related to the number of nodes of the corresponding nonadiabatic vibrational wave functions.

When the LIF spectra were assigned, the energies of the $A-b$ complex levels were calculated using the experimental $D,C\rightarrow A-b$ frequencies and D,C rovibronic term values. Due to numerous perturbations in the $D\,^1\Pi$ state the relevant experimental term values obtained in Ref. [18] were used. $C\,^1\Sigma^+$ state term values were calculated using the PEC from Ref. [19]. The spectra excited with the Ar$^+$ laser lines pro-
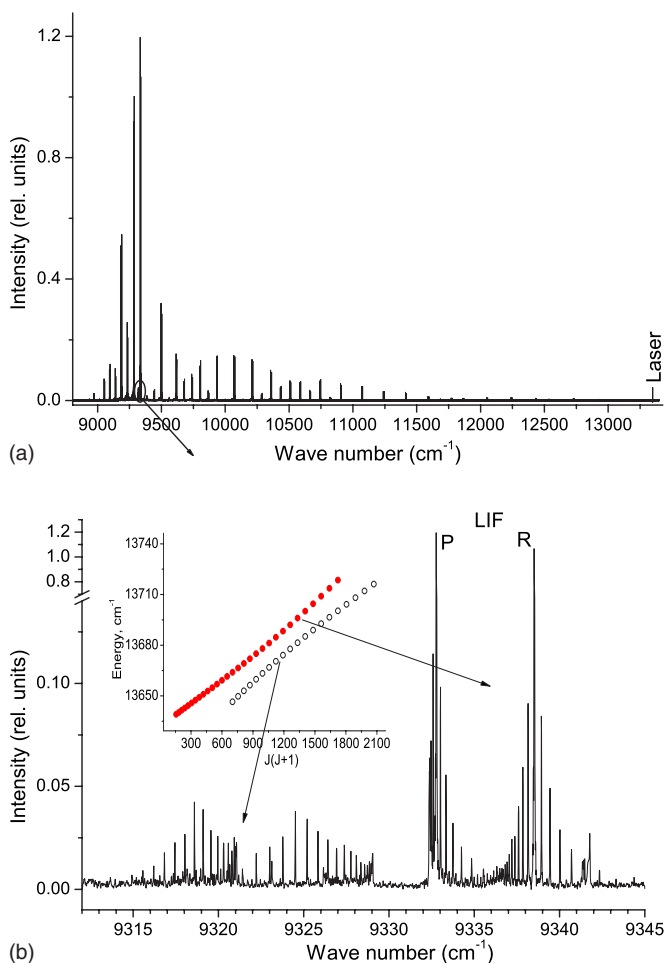
(a)

(b)

FIG. 3. (Color online) $Na^{85}Rb$ $A\,^1\Sigma^+ - b\,^3\Pi \to X\,^1\Sigma^+$ LIF spectrum excited with the Ti:Sa laser at 13 348.847 cm^{-1}. The exciting transition is $X\,^1\Sigma^+(v''_X=2, J''_X=30) \to A\,^1\Sigma^+(v^*_X=30, J'=31)$. (a) The $A \to X$ progression; the region exceeding $\sim$12 000 cm^{-1} was suppressed by a long pass filter. (b) Magnified part [encircled in (a)] of the spectrum with collisionally induced P and R satellite lines. The LIF P and R lines correspond to $(v^*_A=30; J'=31) \to (v''_X=51; J''_X=30, 32)$ transitions. The right group of satellites corresponds to transitions from the $A-b$ levels with predominantly singlet character while the left one—with triplet character. The inset shows the derived experimental term values of the mutually perturbed singlet-triplet levels of the $A-b$ complex as a function of $J'(J'+1)$. Energies are given with respect to the potential minimum of the ground state.

vided rovibronic term values of the $A-b$ complex in the range $v^*_A \in [0,42]$.

The rich rotational relaxation structure observed for the strong $D\,^1\Pi, C\,^1\Sigma^+ \to A\,^1\Sigma^+ - b\,^3\Pi$ progressions provided extensive additional information on the $A-b$ complex since each relaxation of the upper D, C levels leads to a vibrational progression to the full manifold of the $A-b$ complex. Analysis of the $D, C \to A-b$ relaxation lines was used to confirm the rotational assignment by calculating the term values of the same $A-b$ levels from P, R, and Q relaxation lines. A detailed explanation of the relaxation structure in the $^1\Pi \to\, ^1\Sigma^+$ transition can be found in Ref. [18].
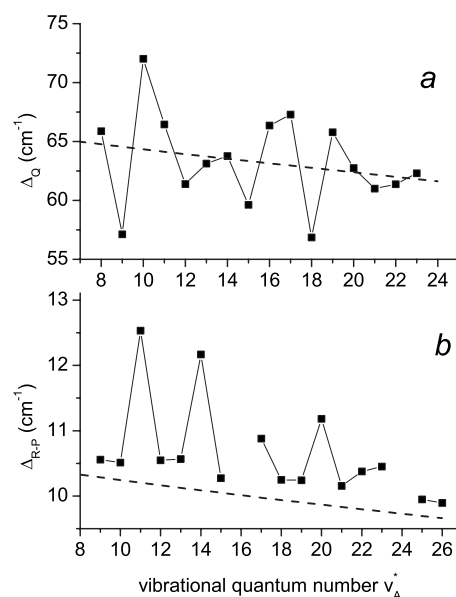

FIG. 4. Irregularities in the vibrational and rotational spacing of the strongly perturbed $Na^{85}Rb$ $D\,^1\Pi \to A\,^1\Sigma^+ - b\,^3\Pi$ LIF progressions excited with the Ar^+ laser line 488.0 nm. (a) Vibrational spacings $\Delta_Q = \nu(v^*_A, J''=25) - \nu(v^*_A+1, J''=25)$ of the progression $D\,^1\Pi(v'=12, J'=25) \to A\,^1\Sigma^+(v^*_A, J''=25)$. (b) Rotational spacings $\Delta_{R-P} \approx B_{v^*_A}(4J''+2)$ of the progression $D\,^1\Pi(v'=13, J'=56) \to A\,^1\Sigma^+(v^*_A; J''=55, 57)$. Dashed lines show the expectations from the present deperturbed $A\,^1\Sigma^+$ state.

The $A\,^1\Sigma^+ - b\,^3\Pi \to X\,^1\Sigma^+$ spectra excited with a Ti:sapphire laser were easily assigned by the ground state PEC [17,20]. Term values of the $A-b$ complex in the range $v^*_A \in [22,49]$ were obtained. Again, the data field of the excited complex was substantially enlarged with the help of the rotational relaxation lines. Most of the laser excited levels have a predominantly singlet character while there are only a few cases where the fluorescence from the levels with dominating triplet character has been observed. Figure 3(b) represents the situation when the population of the optically excited level $v^*_A=30, J_A=31$ is collisionally distributed among the rotational levels of singlet and triplet character. As a result, two groups of relaxation lines were observed—one surrounding the LIF lines coming from the optically excited singlet level and the other, having no clear central lines, starting from the triplet levels. We were able to observe also the opposite situation: optical excitation of a predominantly triplet level and observation of both triplet and singlet relaxation lines.

The full data set of the experimental term values currently available for the NaRb $A-b$ complex is given in EPAPS [30]. The present and previous [21] data are also represented in Fig. 5, which allows us to check the consistency of the data obtained from the different sources. In particular, we have discovered that 26 term values obtained in Ref. [21] for levels $v^*_A \in [6,9]$ should be shifted by 5 cm^{-1} to lower energies. This shift could be attributed to a systematic error of the misaligned Autoscan II wavemeter output during one measurement session. This systematic error could not be recognized in the previous study [21] due to the very limited data
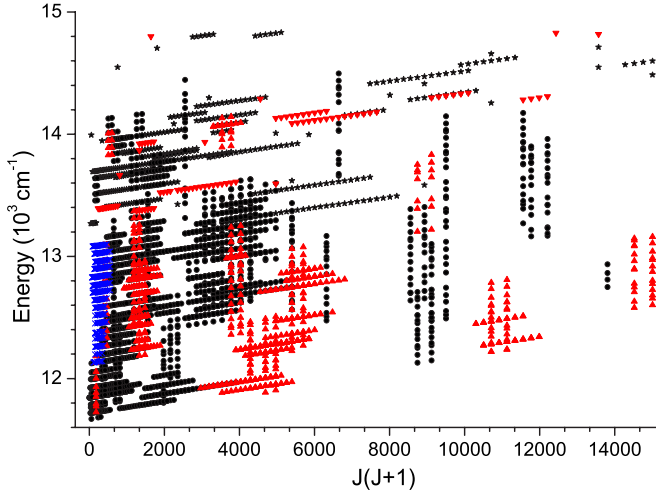
FIG. 5. (Color online) The experimental rovibronic term values of the NaRb $A-b$ complex. Full circles (black) denote the data of Na^{85}Rb and up triangles (red) of Na^{87}Rb obtained from the present measurements. Crosses (blue) show the data of Na^{85}Rb from Ref. [21]. To enlarge the displayed area of the figure for low J a few term values with the highest J values are not presented.

set and the strong local perturbations observed for the low-lying vibrational levels.

The main uncertainty of the FTS term energies derived from the $A\,^1\Sigma^+-b\,^3\Pi\rightarrow X\,^1\Sigma^+$ spectra comes from the Doppler effect. It has been already discussed [18,19] that excitation of a molecular sample with a single mode laser and observation of the fluorescence in a direction parallel to the laser beam leads to a fluorescence, which does not suffer from Doppler broadening. The line frequencies, however, can be shifted from the Doppler-free values within the Doppler profile. As a result, the overall uncertainty of determining the absolute term values from the transition frequencies is generally limited by the Doppler broadening. This is about 0.03 cm^{-1} FWHM in the visible spectral region, diminishing to 0.01 cm^{-1} for 6000 cm^{-1} transitions for the typical working temperatures. Therefore, we estimate the experimental uncertainty as 0.01–0.015 cm^{-1} for the levels obtained from the $A\,^1\Sigma^+-b\,^3\Pi\rightarrow X\,^1\Sigma^+$ spectra. The uncertainty of the term values obtained from the $D\,^1\Pi, C\,^1\Sigma^+\rightarrow A\,^1\Sigma^+-b\,^3\Pi$ spectra can also be estimated as 0.01 cm^{-1}, because energies are calculated from the experimental $D\,^1\Pi$ state term values [18] (accuracy 0.01 cm^{-1} for the reasons described above) and calculated $C\,^1\Sigma^+$ state term values (accuracy 0.01 cm^{-1} stemming from the experimental uncertainty and potential fit quality [19]).

It should be noted that the experimental data field has been further extended and refined (more than 400 term values were added) by a "prediction-correction" iterative procedure arranged as follows. The initial set of the experimental term values was used first to obtain a trial set of deperturbed molecular parameters, which were employed to estimate wave numbers and intensities for the relatively weak $D\,^1\Pi, C\,^1\Sigma^+\rightarrow A\,^1\Sigma^+-b\,^3\Pi$ LIF series unassigned yet. Most of the predicted transitions were then identified in the observed spectra and their experimentally determined frequencies were added to the data set. The enlarged experimental

set was involved in the deperturbation treatment again to refine the parameters of the model and to obtain new term value predictions and identifications of transitions. The procedure has been repeated until the largest possible set of observations was included.

III. CHANNEL-COUPLING DEPERTURBATION ANALYSIS OF THE $A-b$ COMPLEX

A. Outline of the method

Rovibronic levels of the singlet-triplet $A-b$ complex of the NaRb molecule correspond to the intermediate "**a**-**b**-**c**" Hund's coupling case [28,29] since the off-diagonal $A\,^1\Sigma^+-b\,^3\Pi$ SO function value $\xi_{Ab}^{so}(R)$ is comparable with the vibrational spacing of the isolated A state $[\xi_{Ab}^{so}(R_e^A) \simeq \omega_e^A]$ near its equilibrium distance R_e^A while the SO splitting of the triplet state $A_{b\,^3\Pi}^{so}(R)$ is comparable with the electronic-rotation matrix elements between the $b\,^3\Pi_{\Omega=0,1,2}$ components $[A_{b\,^3\Pi}^{so}(R_e^b) \simeq B_e^b\sqrt{2J(J+1)}]$ (where B_e^b is the equilibrium rotational constant of the triplet state) for rotational levels $J \approx 45$ [15,21]. Therefore, the conventional effective Hamiltonian approach [27] is not well suited for the comprehensive deperturbation treatment of the $A-b$ complex due to unavoidable truncation of the space of the rovibrational states for the inverse problem.

In the framework of the alternative channel-coupling (CC) approach [31] the total nonadiabatic rovibronic wave function with the fixed quantum number J of total angular momentum and well-defined total e/f parity can be represented by the linear combination $\sum_{i=1}^{M}\phi_i\varphi_i^{e/f}$ of the electronic-rotational basis wave functions $\varphi_i^{e/f}$ corresponding to a pure Hund's coupling case (**a**) or (**c**) [28]. Here M denotes the total number of electronic substates (channels) explicitly involved in the nonadiabatic treatment. The mixing coefficients ϕ_i of the expansion above determine the nonadiabatic vibrational wave functions, which are solutions of the close-coupling radial equations defined on the infinite interval of the internuclear distance $R \in\,]0,\infty[$,

$$\left(-\mathbf{I}\frac{\hbar^2 d^2}{2\mu dR^2} + \mathbf{V}^{e/f}(R;\mu,J,a_p) - \mathbf{I}E_j^{CC}\right)\mathbf{\Phi}_j = 0, \quad (1)$$

where $\hbar$ is Planck's constant, μ is the reduced molecular mass, $\mathbf{I}$ is the identity matrix, and E_j^{CC} is the rovibronic (total) nonadiabatic energy of the jth level. The fractional radial channel functions $\phi_i(R)$ fulfill the usual boundary $\phi_i(0) = \phi_i(\infty)=0$ and normalization $\sum_{i=1}^{M}\int_0^{\infty}\phi_i^2 dR=1$ condition.

The $M\times M\mathbf{V}^{e/f}$ matrix of potential energy is an explicit function of R depending on the molecular parameters a_p, which will be determined iteratively in the framework of the weighted nonlinear least-squared procedure [28],

$$\min\left\{\sum_{j=1}^{N_{obs}} w_j\delta_j^2/(N_{obs}-n)\right\}, \quad (2)$$

$$\delta_j = E_j^{CC}(a_1,\dots,a_n) - E_j^{expt}, \quad (3)$$

where $w_j=1/\sigma_j^2$ is the weight of each level, E_j^{expt} its experimental term value, and σ_j its uncertainty, N_{obs} is the number

of measurements while n is the total number of adjusted fitting parameters of the deperturbation model used. The minimum of the function (2) is efficiently searched by the modified Levenberg-Marquardt algorithm [32] where first partial derivatives of the eigenvalues E_j^{CC} with respect to the molecular parameters a_i are evaluated by means of the diagonal Hellmann-Feynman theorem [28],

$$\frac{\partial E_j^{CC}}{\partial a_i} = \left\langle \mathbf{\Phi_j} \left| \frac{\partial \mathbf{V}}{\partial a_i} \right| \mathbf{\Phi_j} \right\rangle. \tag{4}$$

The robust weighting procedure [33]

$$w_j = \frac{1}{\sigma_j^2 + \delta_j^2/3} \tag{5}$$

will be useful in the initial stages of the fitting procedure (2) to diminish an undesirable effect of strongly perturbed or/and incorrectly assigned lines. Here, δ_j is the deviation observed on the preceding fit iteration.

B. Model Hamiltonian

The symmetrized electronic-rotational basis wave functions with well-defined parity and corresponding to a pure Hund's coupling case (**a**) [28] are used to represent the NaRb $A\,^1\Sigma^+ - b\,^3\Pi - c\,^3\Sigma^+ - B\,^1\Pi$ complex converging to the common Na(3s)+Rb(5p) dissociation limit (Fig. 1) for a couple of reasons. First, relativistic effects are not dominant in the NaRb molecule and the (**a**) case **V** matrix is symmetric since it does not contain non-Hermitian radial coupling matrix elements appearing in the (**c**) case. Second, the available *ab initio* PECs, spin-orbit coupling, and transition dipole matrix elements are evaluated on nonrelativistic electronic wave functions only [15,21–23]. Overall six independent channels are needed to represent the full $^1\Sigma^+ - ^3\Pi - ^3\Sigma^+ - ^1\Pi$ complex. The total $6 \times 6\,\mathbf{V}$ potential energy matrix corresponding to e and f parity levels of the complex [34] is given in EPAPS [30]. The rotational part of the **V** matrix is evaluated by Eq. (3.2.15) of Ref. [28] assuming that the diagonal angular momentum matrix elements $L_i(L_i+1)=2$ for all states of the p complex according to van Vleck's pure precession hypothesis. The spin-rotation, spin-spin, and hyperfine interactions were neglected in the Hamiltonian. It should be noted that the $\mathbf{V}^f$ matrix does not contain the $A\,^1\Sigma^+$ state, and hence, the low-lying f-parity $b\,^3\Pi_{0,1,2}$ rovibronic levels belonging to the $B-b-c$ complex would be reachable only from the upper states having pronounced triplet character.

Hereafter, we assume that the remote $c\,^3\Sigma^+$ and $B\,^1\Pi$ states (Fig. 1) perturb negligibly the low and intermediate vibrational levels of the reduced $A-b$ complex observed in the present experiment. In this case the truncated 4×4 matrix $\mathbf{V}^e$ has the form

$$V_{^1\Sigma^+} = U_A + B[X+2], \tag{6}$$

$$V_{^3\Pi_0} = U_{b0} + B[X+2], \tag{7}$$

$$V_{^3\Pi_1} = U_{b0} + A^{so} + B[X+2], \tag{8}$$

$$V_{^3\Pi_2} = U_{b0} + 2A^{so} + B[X-2], \tag{9}$$

$$V_{^3\Pi_0 - ^3\Pi_1} = -B\sqrt{2X}, \tag{10}$$

$$V_{^1\Sigma^+ - ^3\Pi_0} = -\sqrt{2}\xi_{Ab}^{so}, \tag{11}$$

$$V_{^3\Pi_1 - ^3\Pi_2} = -B\sqrt{2(X-2)}, \tag{12}$$

$$B \equiv \frac{\hbar^2}{2\mu R^2}, \quad X \equiv J(J+1), \tag{13}$$

where the effective quasirelativistic PEC $U_{b0}=U_b-A^{so}$ was introduced for the $b\,^3\Pi_0$ component to diminish the expected correlation between the original nonrelativistic PEC and A^{so} function because only few experimental data of the $b\,^3\Pi_1$ component are available. It should be pointed out that all molecular parameters of the present deperturbation model, including the BO PECs, are assumed to be mass invariant. The asymptotic behavior of the $\Omega=1$ component is not correct in the four-channel model, since the nonzero SO interaction of the $b\,^3\Pi_1$ component with the $c\,^3\Sigma_1^+$ and $B\,^1\Pi_1$ substates is neglected. For low rotational levels the electronic-rotation interaction between the $\Omega=0,1,2$ components of the $b\,^3\Pi$ state can also be neglected and then, the $\mathbf{V}^e$ matrix can be reduced into the simple two-channels form used in Ref. [21].

C. Analytical representation of electronic matrix elements

It is well known that having an analytical representation of matrix elements for a deperturbation model improves efficiency of the nonlinear least-squares procedure (2) significantly due to analytical calculation of the Jacobian matrix. For this reason, the diagonal $A^{so}(R)$ and the off-diagonal $\xi_{Ab}^{so}(R)$ spin-orbit functions involved in the four-channel model [Eqs. (6), (7), and (9)–(13)] were approximated by the three-parameters Lippincott function [35] converging to the correct atomic limit

$$\xi_{Rb}^{so} - D^{so}e^{-\beta^{so}(R-R^{so})^2/2R}, \tag{14}$$

where $\xi_{Rb}^{so} = [E_{^2P_{3/2}} - E_{^2P_{1/2}}]/3$ is the spin-orbit splitting of the Rb atom in the $5\,^2P$ state [36]. The initial D^{so}, β^{so}, and R^{so} parameters were obtained by fitting Eq. (14) to the *ab initio* points from Ref. [21].

The BO PECs of the interacting $A\,^1\Sigma^+$ and $b\,^3\Pi_0$ states were represented at short $R < R_l$, long $R > R_r$, and intermediate $R_l \leq R \leq R_r$ internuclear distance by the piecewise analytical forms

$$U_l(0 < R < R_l) = \frac{A_l}{R^{\alpha_l}} + B_l, \tag{15}$$

$$U_r(R > R_r) = T^{dis} - U_{ex} - \frac{C_6}{R^6} - \frac{C_8}{R^8},$$
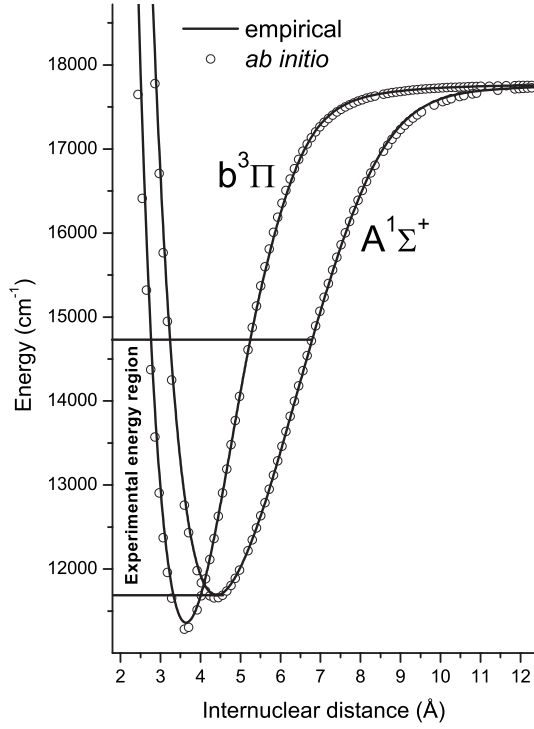
$$U_{ex} = A_r R^{\alpha_r} e^{-\beta_r R}, \tag{16}$$

FIG. 6. The present empirical and *ab initio* [22] Born-Oppenheimer potential energy curves for the deperturbed $A\ ^1\Sigma^+$ and $b\ ^3\Pi$ states.

$$U_G(R_l \leqslant R \leqslant R_r) = T^{dis} - D_e y[2 - y],$$

$$y = \left(\frac{R_e}{R}\right)^p \left(1 + \sum_{i=1}^{N} a_i x_p^i\right), \qquad (17)$$

where

$$x_p = \frac{(R/R_e)^p - 1}{(R/R_e)^p + 1}, \qquad x_p \in \ ]-1,1[\qquad (18)$$

is the reduced coordinate [37], D_e is the well depth, R_e is the equilibrium distance, U_{ex} is the exchange term, and T^{dis} is the dissociation limit referred to the minimum of the ground state. The noninteger degree $p > 1$ of the reduced variable x_p is considered here as an adjustable fitting parameter, which is not directly related to a fixed long range potential degree n. The initial parameters of the $U_G(R)$ potential (17) taken in the modified Gruebele's form [38] were estimated for both states using the BO RKR potentials from Ref. [21]. The fixed $T^{dis}_{b0} = D^X_e + \Delta E_{\text{Rb}} + \xi^{so}_{\text{Rb}}$ and $T^{dis}_A = T^{dis}_{b0} + \xi^{so}_{\text{Rb}}$ values were calculated from the ground state well depth $D^X_e = 5030.502$ cm^{-1} [20] and experimental transition energy [without hyperfine structure (hfs) splitting] $\Delta E_{\text{Rb}} = 12\,578.8741$ cm^{-1} of the Rb atom $5^2P_{1/2}$-$5^2S_{1/2}$ transition [36].

It should be pointed out that only the $U_G(R)$ function of the total PEC could be determined directly from the experimental term values since the left and right matching points (R_l and R_r) were selected to be outside the experimental region limited by observed energies (Fig. 6). Thus, the dispersion coefficients C_6, C_8 of both states were fixed on their

nonrelativistic *ab initio* values [39] whereas the three free parameters for each U_l and U_{ex} function were determined by the boundary conditions

$$\frac{d^i U_{l,r}}{dR^i} = \left.\frac{d^i U_G}{dR^i}\right|_{R=R_{l,r}}, \quad i = 0,1,2, \qquad (19)$$

which guarantees smoothness of the resulting PECs up to the second derivative with respect to R at the matching points.

D. Analytical mapping procedure

The direct deperturbation analysis is a rather time consuming process due to a tedious solution of the close-coupling equations. Therefore, it is of importance to optimize the computational procedures involved. In this section we discuss an efficient mapping procedure, which enables one to reduce significantly the number of grid points on the R axis for solving the system of coupled equations.

The reduced z variable, defined on the finite interval $z \in \ ]0,1[$ by the two parameters ρ, γ in the analytical form,

$$z(R) = \frac{1}{1 + \left(\dfrac{\rho}{R}\right)^\gamma}, \quad \rho > 0, \quad \gamma > 1, \qquad (20)$$

was used to transform exactly the original R-dependent CC equations (1) to the Hermitian z-dependent form [40],

$$-\frac{\hbar^2}{2\mu}\mathbf{G}\left(\frac{d^2\boldsymbol{\Psi}}{dz^2}\right)\mathbf{G} = [\mathbf{I}E^{CC} - \mathbf{V} + \mathbf{I}f]\boldsymbol{\Psi}, \qquad (21)$$

where $\mathbf{G} = \mathbf{I}g$ is a diagonal matrix, $\boldsymbol{\Psi} = \dfrac{\boldsymbol{\Phi}}{\sqrt{g}}$, and

$$g \equiv \frac{dz}{dR} = \frac{\gamma}{\rho}z^{1-(1/\gamma)}(1 - z)^{1+(1/\gamma)} > 0, \qquad (22)$$

$$f = \frac{1 - \gamma^2}{4\rho^2}\left(\frac{1 - z}{z}\right)^{2/\gamma}. \qquad (23)$$

The modified equations (21) were solved by the finite-difference (FD) boundary value method [41] using the central five-point FD approximation of the second derivative term d^2/dz^2. The ordinary eigenvalue problem of the resulting symmetric band matrix was solved by the implicitly restarted Lanczos method taken in the shift-inverted spectral transformation mode [42]. The eigenvalues $E^{CC}_{j,1}, E^{CC}_{j,2}$ obtained for $N_1 = 1024$ and $N_2 = 1536$ numbers of the uniformly distributed z points were extrapolated to zero step $E^{CC}_j(h \to 0) \approx E^{CC}_j + \Delta E^{CC}_j$ assuming h^4 dependence of the discretization error $\Delta E^{CC}_j = [E^{CC}_{j,2} - E^{CC}_{j,1}]/[(N_1/N_2)^4 - 1]$.

In accordance with the well-known WKB approximation [43] the ideal substitution function $z(R)$ should yield the first derivative dz/dR close to the momentum $k(R) = \sqrt{2\mu|E - U|}/\hbar$ in the classically allowed region of motion. Therefore, the ρ and γ parameters of the mapping function (20) appropriate for the lowest vibrational levels could be estimated by the condition

$$\frac{d^i g}{dR^i} = \left. \frac{d^i k}{dR^i} \right|_{R=R_e}, \quad i = 1, 2, \tag{24}$$

yielding to

$$\gamma \approx \sqrt{1 + \frac{\omega_e}{B_e(2v+1)}}, \quad \rho \approx R_e \left(\frac{\gamma+1}{\gamma-1} \right)^{1/\gamma} \tag{25}$$

for the harmonic oscillator model.

The trial mapping parameters $\gamma_A = 5.4$, $\gamma_b = 6.5$ and $\rho_A = 4.8$ Å, $\rho_b = 3.9$ Å of the isolated A and b states were estimated by Eq. (25) for the intermediate vibrational levels $v_A = 25$ and $v_b = 18$, respectively. Then, the geometric means $\gamma_{A-b} = \sqrt{\gamma_A \gamma_b} = 5.9$ and $\rho_{A-b} = \sqrt{\rho_A \rho_b} = 4.3$ Å were supposed to be initially optimal for the close-coupling calculations and were refined by the minimization of the overall discretization error $\Sigma_{j=1}^{N_{obs}}(\Delta E_j^{CC})^2/(N_{obs}-2)$.

The resulting $\gamma_{A-b} = 6.2$ and $\rho_{A-b} = 4.6$ Å values lead to the mean absolute error in the extrapolated $E_j^{CC}(h \to 0)$ eigenvalues of the order of 10^{-5} cm^{-1}. It should be pointed out that the minimum number of uniformly distributed R-coordinate points required to achieve the same accuracy is 3.5 times larger than the uniformly distributed z points. In comparison with the numerical mapping procedure of Refs. [44,45] the present analytical method introduces no numerical approximation due to a precise calculation of the required reciprocal $R = \rho[z/(1-z)]^{1/\gamma}$, mapping $g(z)$ [Eq. (22)] and auxiliary $f(z)$ [Eq. (23)] functions while both analytical and numerical approaches have almost the same efficiency.

IV. RESULTS FOR MOLECULAR POTENTIALS AND SPIN-ORBIT PARAMETERS

From the FTS analysis and previously published data [21] we derived a data set of about 2300 highly accurate experimental term values E_j^{expt} for $4 \leq J \leq 163$ belonging to the e-parity component of the mutually perturbed rovibronic $A\,^1\Sigma^+$ and $b\,^3\Pi$ levels of both Na^{85}Rb and Na^{87}Rb isotopomers. The input data field consists mostly of singlet $A\,^1\Sigma^+(0 \leq v_A^* \leq 49)$ levels and a considerable number (>360) of predominantly triplet $b\,^3\Pi_0$ and even $b\,^3\Pi_1$ sublevels (see the corresponding mixing coefficients in [30]). These energies were simultaneously involved in the iterative fitting procedure (2) by using the inverted four-coupled-channels approach (4×4ICCA). Overall, 24 mass-invariant fitting parameters (see Table I and Ref. [30]) were required to define the BO potential energy curves $U_{A\,^1\Sigma^+}$, $U_{b\,^3\Pi}$ (Fig. 6) and spin-orbit coupling functions $A_{b\,^3\Pi}^{so}$, ξ_{Ab}^{so} (Fig. 7). One should keep in mind that the exchange function U_{ex} was solely used to provide a smooth connection between the long range and U_G parts of the PEC and, hence, the derived A_r, α_r, and β_r parameters (Table I) should not be interpreted in its usual physical meaning. The present deperturbation model defined by Eqs. (6)–(13) reproduces the 2311 experimental term values of the $A\,^1\Sigma^+$–$b\,^3\Pi$ complex for both isotopomers with a standard deviation of 0.012 cm^{-1} close to the estimated uncertainty of the FTS measurements of 0.01 cm^{-1}.

TABLE I. The mass-invariant parameters of the empirical potential energy curves (15)–(17) and spin-orbit coupling functions (14) derived for the deperturbed $A\,^1\Sigma^+$ and $b\,^3\Pi_0$ states of the NaRb molecule by the direct inverted four-channel-coupling approach.

	$A\,^1\Sigma^+$ state	$b\,^3\Pi_0$ state
The intermediate range potential Eq. (17)		
T^{dis} [20,36] (cm^{-1})[a]	17767.825	17688.601
D_e (cm^{-1})	6079.539	6377.559
R_e (Å)	4.400357767	3.634872298
p	2.883208647	6.824399015
a_1	0.6366497649	1.285050816
a_2	-0.1712229898	0.6476081431
a_3	-0.2966081503	0.4877347492
a_4	-1.289466410	0.3087764448
a_5	-1.838692770	0.3206376730
a_6	-0.7715827075	0.3234481049
a_7	0.9098596994	0.1713686756
The short-range potential Eq. (15)		
R_l (Å)[a]	3.1	2.6
A_l (cm^{-1} Å$^\alpha$)	2.58522×10^5	3.46813×10^5
B_l (cm^{-1})	7177.885	7919.657
α_l	3.006516818	3.873726877
The long-range potential Eq. (16)		
R_r (Å)[a]	7.5	5.5
C_6 [39] (cm^{-1} Å^6)[a]	8.97417×10^7	3.60707×10^7
C_8 [39] (cm^{-1} Å^8)[a]	4.00024×10^9	2.97309×10^8
A_r (cm^{-1}/Å$^\beta$)	$-2.15138574 \times 10^{-13}$	$-1.824582991 \times 10^{-13}$
α_r	39.6495986	52.68444083
β_r (1/Å)	5.83690903	9.788335902
	ξ_{Ab}^{so}	$A_{b\,^3\Pi}^{so}$
The spin-orbit functions Eq. (14)		
D^{so} (cm^{-1})	37.8445	38.5542
R^{so} (Å)	4.80067[a]	4.453253784
β^{so} (1/Å)	0.84969[a]	2.942367838
ξ_{Rb}^{so} [36] (cm^{-1})[a]		79.2242

[a]Fixed parameter.

Table II demonstrates that the state-of-art accuracy of *ab initio* MPPT and CPP PECs is basically limited in the electronic energy T_e by several hundred cm^{-1}. More accurate estimates for the excited states are often obtained by the so-called "difference-based" potentials $U^{dif} = [U_i^{ab} - U_X^{ab}] + U_X^{emp}$ [23] using the empirical ground state PEC U_X^{emp} [20] and the theoretical potentials U_i^{ab}, U_X^{ab} obtained by the same computational procedure. However, recent CPP PECs from Ref. [22] seem to be most accurate; their consistence with present empirical PECs is remarkable even outside the experimental data region (Fig. 6). Thus the proposed short- and long-range extrapolation might be useful for further calculations involving the $B\,^1\Pi$ and $c\,^3\Sigma^+$ states in order to refine the asymptotic behavior of the $\Omega = 1$ states manifold.

Both diagonal $A_{b\,^3\Pi}^{so}$ and off-diagonal ξ_{Ab}^{so} empirical SO coupling functions are larger than their *ab initio* counterparts
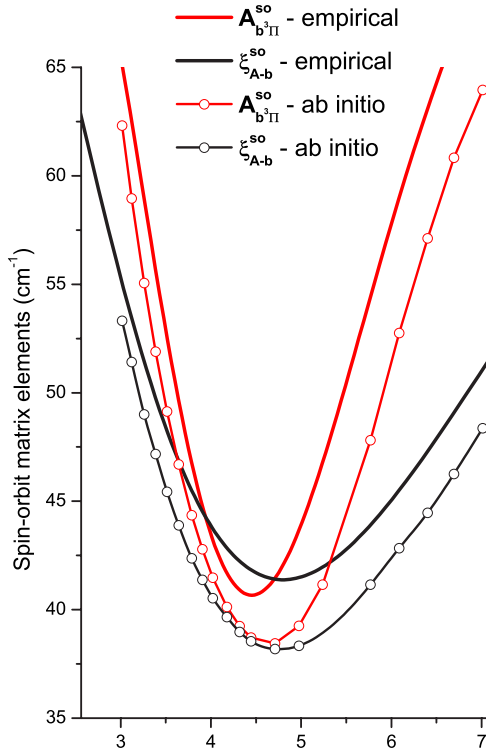
FIG. 7. (Color online) The present empirical and *ab initio* [21] spin-orbit $A^{so}_{b\,^3\Pi}(R)$, $\xi^{so}_{Ab}(R)$ functions.

TABLE II. The electronic energy T_e (in cm^{-1}) and equilibrium distance R_e (in Å) available for the $A\,^1\Sigma^+$ and $b\,^3\Pi$ states of the NaRb molecule from the *ab initio* U^{ab}, difference-based U^{dif} and empirical U^{emp} BO PECs.

	$A\,^1\Sigma^+$		$b\,^3\Pi$	
Source	T_e	R_e	T_e	R_e
Ab initio				
CPP [15]	11396	4.47	11303	3.70
CPP [22]	11680	4.38	11308	3.61
MPPT [23]	11708	4.25	11060	3.65
MPPT [21]	12109	4.24	11012	3.63
Difference-based				
CPP [15]	11630	4.38	11300	3.63
CPP [22]	11619	4.39	11309	3.64
MPPT [23]	11596	4.40	11288	3.65
MPPT [21]	11769	4.43	11242	3.65
Empirical				
DPF-HH [25]	11712	4.42		
2×2ICCA-RKR [21]	11702.2	4.406	11307.5[a]	3.64[a]
4×4ICCA-MLJ[b]	11688.5	4.400	11360.7	3.64

[a]Values correspond to the $b\,^3\Pi_{\Omega=0}$ state.
[b]Present.

[21] only by 3–5 cm^{-1} in the experimental data region (Fig. 7). Such a difference can be attributed to a systematic error in the Rb atom pseudopotential estimates [21], which have ignored completely the possible relativistic contribution of the Na atom for the SO matrix elements. It should be noted that the empirical off-diagonal $\xi^{so}_{Ab}(R)$ function could be unambiguously determined from the present data set only in a small R region located near the crossing point R^{PEC}_{Ab} =4.10 Å of the deperturbed $A\,^1\Sigma^+$ and $b\,^3\Pi$ BO PECs (Fig. 6), where overlapping of the corresponding ϕ_A and ϕ_{b0} functions is most pronounced. Therefore, the analytical function $\xi^{so}_{Ab}(R)$ was constrained by fixing R^{so} and β^{so} parameters determined from a fit to the *ab initio* data points from Ref. [21], so D^{so} was the only free parameter in the fit.

V. TRANSITION PROBABILITIES. STIMULATED RAMAN PROCESS $a\,^3\Sigma^+ \to A\,^1\Sigma^+ - b\,^3\Pi \to X\,^1\Sigma^+$

Understanding the intensity distribution in the molecular spectra along with the transition frequencies is a problem, which serves as a test for the extent to which we can model a given molecular system. This is particularly important and challenging in cases like those presented here, where strong mixing of states with different multiplicities takes place and the simplified selection rules for transitions cannot be directly applied. In this section we illustrate the application of our results for modeling the intensity distribution within the $D \to A-b$ and $A-b \to X$ bands. The first case is not trivial due to the changing degree of singlet-triplet admixture of the $A-b$ rovibrational levels, so all four channels of the model

should be used for calculating the correct rovibrational wave functions. In the second case we demonstrate the importance of taking into account the A-X transition dipole moment instead of calculating just Franck-Condon factors.

In the framework of a pure Hund's coupling case "**a**" singlet-triplet electronic dipole transitions are strictly forbidden [28]. Therefore the relative intensity distributions for the observed $D\,^1\Pi \to A\,^1\Sigma^+ - b\,^3\Pi$ (Fig. 8) and $A\,^1\Sigma^+ - b\,^3\Pi \to X\,^1\Sigma^+$ (Fig. 9) [21,25] LIF progressions are given as

$$I^{v'-E^{CC}_j}_{D\to A-b} - (E^{v'}_D - E^{CC}_j)^4|\langle \chi^{v'}_D|d_{DA}|\phi^j_A\rangle -^2, \qquad (26)$$

$$I^{E^{CC}_j-v''}_{A-b\to X} - (E^{CC}_j - E^{v''}_X)^4|\langle \phi^j_A|d_{AX}|\chi^{v''}_X\rangle|^2, \qquad (27)$$

where with the power of four we assume that the detector signal is proportional to the intensity of the incoming fluorescence light. $|\phi^j_A\rangle$ is the singlet character fraction of the nonadiabatic vibrational wave function of energy level E^{CC}_j. The BO energies $E^{v''}_X, E^{v'}_D$ and eigenfunctions $\chi^{v''}_X, \chi^{v'}_D$ were obtained by solving the single channel radial equation with the empirical PECs from Refs. [18,20]. $d_{AX}(R)$, $d_{DA}(R)$ are the *ab initio* A-X and D-A electronic transition dipole moments [21–23].

In Fig. 8 we see a comparison between experimental and calculated relative intensity distributions in a $D\,^1\Pi \to A\,^1\Sigma^+ - b\,^3\Pi$ LIF progression. In the upper graph the intensities were taken as being proportional only to the FCF values calculated with the single channel rovibrational wave functions. In the lower graph the wave functions were obtained within the ICCA model and also the dipole transition moment $d_{DA}(R)$ was taken into account. We see some experi-
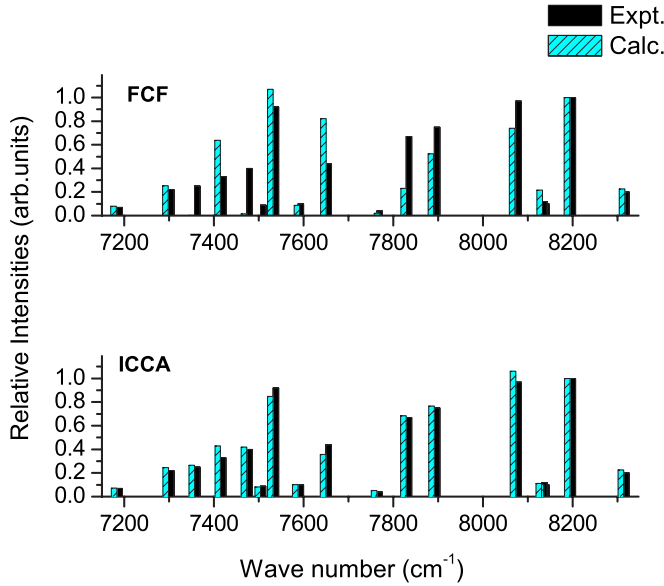
FIG. 8. (Color online) The experimental and calculated relative intensity distributions (normalized at 8200 cm^{-1}) of the $D\ ^1\Pi(v_D^-=30, J^-=50) \rightarrow A\ ^1\Sigma^+ - b\ ^3\Pi$ LIF progression coming to the strongly perturbed levels of the $A-b$ complex for the case of Q lines. FCF: Franck-Condon approximation for pure D-A transitions; ICCA: coupled-channels approach.

mental lines (e.g., around 7500 cm^{-1}) the appearance of which can be understood only within the ICCA model. The results of the $A\ ^1\Sigma^+ - b\ ^3\Pi \rightarrow X\ ^1\Sigma^+$ progression are presented in Fig. 9. Since this progression starts from a weakly perturbed level of the complex, the intensities predicted by the FCFs agree much better with the experimental observations. Nevertheless the apparent disagreement for lower v_X can be overcome only by including the $d_{AX}(R)$ transition dipole mo-
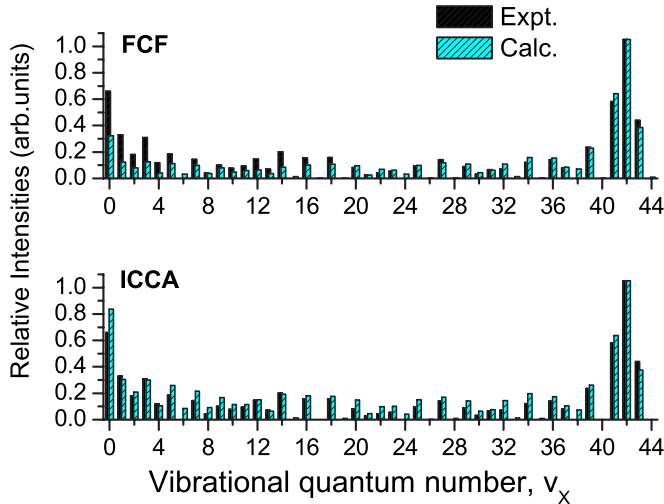

FIG. 9. (Color online) The calculated and experimental [21,25] relative intensity distribution (normalized at $v_X=42$ in the long $A\ ^1\Sigma^+ - b\ ^3\Pi(v_A^*=19, J^-=50) \rightarrow X\ ^1\Sigma^+(v_X^- \in [0,43])$ LIF progression starting from the weakly perturbed level of the complex. The intensities of the P and R lines are averaged. FCF, Franck-Condon approximation for pure A-X transitions; ICCA, coupled-channels approach.

ment function as done in the ICCA calculations.

Proven the quality of the model for describing correctly not only frequencies but also the line intensities of transitions to and from the $A-b$ complex we applied it for accurate simulation of stimulated Raman processes $a \rightarrow A-b \rightarrow X$, which lead to efficient formation of ultracold NaRb molecules in their ground level $v_X''=0$; $J_X''=0$ from initial $a\ ^3\Sigma^+(N''=0)$ levels located near the atomic ground state asymptote.

The rovibronic transition probabilities of the stimulated Raman $a\ ^3\Sigma^+(N''=0) \rightarrow A\ ^1\Sigma^+ - b\ ^3\Pi(E_j^{CC}; J'=1) \rightarrow X\ ^1\Sigma^+(v_X''=0; J_X''=0)$ PUMP-DUMP process is proportional to the product $(M_{A-X}^{E_j^{CC}-v_X''})^2 (M_{b_0-a}^{E_j^{CC}-v_a''} + M_{b_1-a}^{E_j^{CC}-v_a''})^2$, where the transition dipole moments between the $A\ ^1\Sigma^+ - b\ ^3\Pi$ complex and the low-lying $X\ ^1\Sigma^+$, $a\ ^3\Sigma^+$ states (see Fig. 1) are given by

$$M_{A-X}^{E_j^{CC}-v_X''} = \langle \phi_A^j | d_{AX} | \chi_X^{v''} \rangle S_{J'J''}^{\Omega'\Omega''}, \tag{28}$$

$$M_{b_\Omega-a}^{E_j^{CC}-v_a''} = \langle \phi_{b_\Omega}^j | d_{ba} | \chi_a^{v''} \rangle S_{J'J''}^{\Omega'\Omega''}. \tag{29}$$

Here, $S_{J'J''}^{\Omega'\Omega''}$ is the analytically known overlap integral between rotational wave functions [28]. The $|\phi_A^j\rangle, |\phi_{b_\Omega}^j\rangle$ are, respectively, the $A\ ^1\Sigma^+$ and $b\ ^3\Pi_{\Omega'=0,1,2}$ fractions of the nonadiabatic vibrational wave function of energy level E_j^{CC} while the $d_{AX}(R), d_{ba}(R)$ are, respectively, the A-X and b-a electronic transition dipole moments [21,22]. The $|\chi_{X,a}^{v''}\rangle$ are the BO eigenfunctions of the isolated ground $X\ ^1\Sigma^+$ and $a\ ^3\Sigma^+$ states obtained by solving the single channel radial equation with the empirical PECs from Ref. [20].

The radiative lifetimes of the intermediate $A\ ^1\Sigma^+ - b\ ^3\Pi(E_j^{CC}; J'=1)$ levels are estimated as the expectation value [46]

$$\frac{1}{\tau_{A-b}^{E_j^{CC}}} = \frac{8\pi^2}{3\hbar c} \int_0^\infty dR$$

$$\times \left[(\phi_A^j)^2 \Delta U_{AX}^3 d_{AX}^2 + \left(\sum_{\Omega=0,1} (\phi_{b_\Omega}^j)^2 \right) \Delta U_{ba}^3 d_{ba}^2 \right], \tag{30}$$

where $\Delta U_{ij}(R) = U_i(R) - U_j(R)$ is the difference of the BO PECs; for $J'=1$ $\Omega=2$ does not play a role. The branching ratio of the spontaneous emission from the intermediate level to the ground level $v_X''=0$; $J_X''=0$ is defined as

$$R_{A-b}^{E_j^{CC}} = A_{A-b-X}^{E_j^{CC}-v_X''} \tau_{A-b}^{E_j^{CC}} \tag{31}$$

with the spontaneous decay rate to v_X'' of the singlet ground state

$$A_{A-b-X}^{E_j^{CC}-v_X''} = \frac{8\pi^2}{3\hbar c} (E_j^{CC} - E_X^{v''})^3 (M_{A-X}^{E_j^{CC}-v_X''})^2.$$

The selected excitation $\nu_{a \rightarrow A-b}^{PUMP}$ and emission $\nu_{A-b \rightarrow X}^{DUMP}$ transitions corresponding to the most pronounced transition probabilities of the $a\ ^3\Sigma^+ \rightarrow A\ ^1\Sigma^+ - b\ ^3\Pi \rightarrow X\ ^1\Sigma^+$ process are presented in Table III, where squares of the relevant M_{A-X}

TABLE III. The $\nu_{a\rightarrow A-b}^{PUMP}$, $\nu_{A-b\rightarrow X}^{DUMP}$ are the wave numbers of the PUMP-DUMP transitions corresponding to the favorable transition probabilities for the stimulated Raman process $a\,^3\Sigma^+(N''=0)$ $\rightarrow A\,^1\Sigma^+ - b\,^3\Pi(E_j^{CC};J'=1)\rightarrow X\,^1\Sigma^+(v''=0;J''=0)$. The $\nu_{a\rightarrow A-b}^{PUMP}$ values are given with respect to the binding energy of the last bound $v_a''=22$ level of the $a\,^3\Sigma^+$ state, namely, $\Delta^{Na^{85}Rb}\approx -0.003$ and $\Delta^{Na^{87}Rb}\approx -0.004$ cm^{-1}. M_{A-X} and M_{b-a} are the $A-b$-X and $A-b$-a transition moments, respectively. The τ_{A-b} are the radiative lifetimes while R_{A-b} is the branching ratios of the intermediate $A-b$ levels to the ground level $v_X''=0;J_X''=0$. The P_A are the A-state fractions of the total nonadiabatic wave functions.

$\nu_{a\rightarrow A-b}^{PUMP}$ (cm^{-1})	$\nu_{A-b\rightarrow X}^{DUMP}$ (cm^{-1})	$M_{A\text{-}X}^2$ (a.u.)^2	$M_{b\text{-}a}^2$ (a.u.)^2	τ_{A-b} (ns)	R_{A-b} (%)	P_A (%)
Na^{85}Rb						
8112.63	13089.81	2.1(−1)	5.4(−6)	115	11	17
8304.22	13281.41	9.8(−2)	8.1(−6)	67	3	35
7915.25	12892.44	7.0(−1)	9.4(−7)	43	13	53
8016.43	12993.62	1.2(−1)	3.4(−6)	313	16	6
8473.03	13450.22	6.0(−2)	5.5(−6)	38	1	65
8289.57	13266.76	1.2(−1)	2.5(−6)	40	2	66
7740.69	12717.88	7.4(−1)	3.4(−7)	46	14	52
7927.68	12904.87	2.4(−1)	9.2(−7)	55	6	49
8206.85	13184.03	2.7(−2)	7.7(−6)	380	5	6
8232.39	13209.57	3.1(−1)	5.6(−7)	26	4	97
8488.18	13465.37	1.9(−2)	8.0(−6)	73	1	37
8418.81	13396.00	1.2(−1)	1.2(−6)	27	2	93
7860.61	12837.80	9.9(−1)	1.2(−7)	27	11	93
8354.65	13331.84	1.6(−1)	6.1(−7)	26	2	95
8658.42	13635.60	2.4(−2)	4.1(−6)	32	1	74
8108.24	13085.42	1.3(+0)	6.1(−8)	31	5	85
7668.12	12645.31	3.3(−1)	2.3(−7)	25	14	97
7793.99	12771.18	1.2(+0)	5.4(−8)	26	13	94
Na^{87}Rb						
8108.80	13086.11	2.7(−1)	7.3(−6)	83	10	24
8299.96	13277.27	1.0(−1)	1.1(−5)	63	3	38
7912.04	12889.36	6.8(−1)	1.4(−6)	46	14	50
8012.52	12989.84	1.2(−1)	5.0(−6)	321	17	5
8468.56	13445.87	6.0(−2)	8.4(−6)	39	1	63
8285.29	13262.60	1.2(−1)	4.0(−6)	41	2	64
7737.79	12715.11	7.6(−1)	4.6(−7)	44	14	54
7924.05	12901.37	2.7(−1)	1.2(−6)	52	6	52
8202.44	13179.76	2.6(−2)	1.1(−5)	365	4	6
8228.71	13206.02	3.1(−1)	9.0(−7)	26	4	97
8104.44	13081.76	2.1(−2)	1.1(−5)	34	4	77
8483.29	13460.61	2.8(−1)	7.9(−7)	69	1	39
8414.71	13392.03	1.2(−1)	1.6(−6)	27	2	93
7857.71	12835.03	9.9(−1)	1.7(−7)	27	11	93
8350.67	13327.99	1.7(−1)	9.6(−7)	26	2	95
8653.79	13631.11	2.5(−2)	5.9(−6)	33	1	72
7665.73	12643.05	1.3(+0)	9.2(−8)	25	14	97
7791.31	12768.63	1.2(+0)	9.0(−8)	26	13	94

and M_{b-a} transition moments are given for estimating the required laser power of a pure Raman or STIRAP process [16]. Table III also contains the radiative lifetimes and branching ratios predicted for the intermediate levels of the complex. The branching ratios will be useful for estimating the efficiency of the simple one step PUMP-spontaneous emission process for producing the $v_X=0$; $J=0$ population, a 10% contribution could be already significant.

The energy of the initial $a\,^3\Sigma^+(N_a''=0)$ level will be apparently taken to be close to the dissociation energy of the ground state using an ultracold ensemble of Na+Rb as a start in which a loosely bound state of NaRb may be formed by a Feshbach magnetic ramp. In particular, the $|M_{b\text{-}a}|^2$ values presented in Table III were estimated using the space normalized wave function corresponding to the last loosely bound level of the $a\,^3\Sigma^+$ state. In these estimations we neglected the hyperfine structure of the loosely bound levels, which produces singlet-triplet mixing. Taking this into account will not really help because we have no proper estimation of the hyperfine structure of the upper levels, thus the model would remain incomplete.

It should be noted that the relative magnitude of the $|M_{b\text{-}a}|^2$ values within the table column are not very sensitive to a particular energy of the initial $a\,^3\Sigma^+$ state since the nodal structure of their corresponding vibrational wave functions $|\chi_a^{v''}\rangle$ almost coincides near the left turning points of the short-range potential while amplitudes of the wave function and, hence, the absolute $|M_{b\text{-}a}|^2$ values strongly depend on the binding energy [44]. The dump transitions show very large dipole moments but those for the pump transitions are fairly low requiring laser power of 100 mW focused to a waist of 100 μm for obtaining Rabi frequencies in the order of 10 MHz. As a laser source for the dump transition around 770 nm a diode laser or cw Ti:sapphire laser could be used. The pump transition seems to be more difficult to obtain not only because of the high power but due to the unfavorable wavelength. Nevertheless, commercially available diode lasers (e.g., LD-1260-0070-1 by Toptica Photonics) at 1.31 or 1.26 μm or a cw optical parametric amplifier could be applied.

VI. CONCLUSIONS

Overall 24 mass-invariant fitting parameters have been required to reproduce about 2300 experimental term values of the $A-b$ NaRb complex of both isotopomers with a standard deviation of 0.012 cm^{-1} consistent with the uncertainty of the FTS experiment.

The incorporation of a wide range of vibrational levels $(0 \leqslant v_A^* \leqslant 49)$ in the deperturbation procedure allowed us to refine and extend the empirical PECs for both singlet and triplet states significantly compared to Ref. [21]. Moreover, the diagonal spin-orbit splitting function of the $b\,^3\Pi$ state was determined due to pronounced electronic-rotation interaction between the $b\,^3\Pi_{0,1,2}$ components observed for high J

levels and the inclusion in the fit of the experimental data for the $b\,^3\Pi_1$ component.

The analytical mapping procedure based on the reduced variable representation of the radial coordinate reduced the number of grid points required for solving the CC equations by a factor of at least 3.5.

The inclusion of the variable degree parameter p of the reduced variable x_p [Eq. (18)] in the analytical U_G potential representation allowed us to decrease the total number and the absolute values of the polynomial coefficients required to determine the fitted U_G potential.

The relative intensity distributions predicted for the $D \rightarrow A-b$ and $A-b \rightarrow X$ LIF progressions by using the present $A-b$ nonadiabatic wave functions and the available *ab initio* dipole moments [21–23] agree with their experimental counterparts within the accuracy of the measurements.

The present deperturbation analysis, combined with the recent empirical PECs for both low-lying $X\,^1\Sigma^+$, $a\,^3\Sigma^+$ states [20] and relevant $A-X$, $b-a$ *ab initio* transition dipole moments, is useful for rigorous exploration of ultracold NaRb molecule formation in the ground level $v_X=0$; $J_X=0$ by means of stimulated Raman and/or STIRAP processes $a\,^3\Sigma^+ \rightarrow A\,^1\Sigma^+ - b\,^3\Pi \rightarrow X\,^1\Sigma^+$. We give quantitative transition moments for favorable lambda schemes, which show that such experiments are feasible but would need fairly high powers in the near infrared.

[1] K. Goral, L. Santos, and M. Lewenstein, Phys. Rev. Lett. **88**, 170406 (2002).

[2] J. L. Bohn, Phys. Rev. A **63**, 052714 (2001).

[3] D. DeMille, Phys. Rev. Lett. **88**, 067901 (2002).

[4] M. G. Kozlov and L. N. Labzowsky, J. Phys. B **28**, 1933 (1995).

[5] C. A. Stan, M. W. Zwierlein, C. H. Schunck, S. M. F. Raupach, and W. Ketterle, Phys. Rev. Lett. **93**, 143001 (2004).

[6] S. Inouye, J. Goldwin, M. L. Olsen, C. Ticknor, J. L. Bohn, and D. S. Jin, Phys. Rev. Lett. **93**, 183201 (2004).

[7] D. Wang, J. Qi, M. F. Stone, O. Nikolayeva, H. Wang, B. Hattaway, S. D. Gensemer, P. L. Gould, E. E. Eyler, and W. C. Stwalley, Phys. Rev. Lett. **93**, 243005 (2004).

[8] M. W. Mancini, G. D. Telles, A. R. L. Caires, V. S. Bagnato,

and L. G. Marcassa, Phys. Rev. Lett. **92**, 133203 (2004).

[9] C. Haimberger, J. Kleinert, M. Bhattacharya, and N. P. Bigelow, Phys. Rev. A **70**, 021402(R) (2004).

[10] G. D. Telles, L. G. Marcassa, S. R. Muniz, S. G. Miranda, A. Antunes, C. Westbrook, and V. S. Bagnato, Phys. Rev. A **59**, R23 (1999).

[11] Y. E. Young, R. Ejnisman, J. P. Shaffer, and N. P. Bigelow, Phys. Rev. A **62**, 055403 (2000).

[12] G. D. Telles, L. S. Aguiar, L. G. Marcassa, and V. S. Bagnato, Phys. Rev. A **66**, 025403 (2002).

[13] J. M. Sage, S. Sainis, T. Bergeman, and D. DeMille, Phys. Rev. Lett. **94**, 203001 (2005).

[14] W. C. Stwalley, Eur. Phys. J. D **31**, 221 (2004).

[15] M. Korek, A. R. Allouche, M. Kobeissi, A. Chaalan, M. Dagher, K. Fakherddin, and M. Aubert-Frecon, Chem. Phys. **256**, 1 (2000).

[16] K. Bergmann, H. Theuer, and B. W. Shore, Rev. Mod. Phys. **70**, 1003 (1998).

[17] O. Docenko, M. Tamanis, R. Ferber, A. Pashov, H. Knöckel, and E. Tiemann, Phys. Rev. A **69**, 042503 (2004).

[18] O. Docenko, M. Tamanis, R. Ferber, A. Pashov, H. Knöckel, and E. Tiemann, Eur. Phys. J. D **39**, 49 (2005).

[19] W. Jastrzebski, P. Kortyka, P. Kowalczyk, O. Docenko, M. Tamanis, R. Ferber, A. Pashov, H. Knöckel, and E. Tiemann, Eur. Phys. J. D **36**, 57 (2005).

[20] A. Pashov, O. Docenko, M. Tamanis, R. Ferber, H. Knoeckel, and E. Tiemann, Phys. Rev. A **72**, 062505 (2005).

[21] M. Tamanis, R. Ferber, A. Zaitsevskii, E. A. Pazyuk, A. V. Stolyarov, H. Chen, J. Qi, H. Wang, and W. C. Stwalley, J. Chem. Phys. **117**, 7980 (2002).

[22] M. Aymar and O. Dulieu (private communication).

[23] A. Zaitsevskii, S. O. Adamson, E. A. Pazyuk, A. V. Stolyarov, O. Nikolayeva, O. Docenko, I. Klincare, M. Auzinsh, M. Tamanis, R. Ferber, and R. Cimiraglia, Phys. Rev. A **63**, 052504 (2001).

[24] Ch. Lisdat, O. Dulieu, H. Knöckel, and E. Tiemann, Eur. Phys. J. D **17**, 319 (2001).

[25] A. Jarmola, M. Tamanis, R. Ferber, E. A. Pazyuk, and A. V. Stolyarov, J. Quant. Spectrosc. Radiat. Transf. **95**, 165 (2005).

[26] V. V. Meshkov, A. Zaitsevskii, E. A. Pazyuk, A. V. Stolyarov, R. Bruhl, and D. Zimmermann, J. Chem. Phys. **123**, 204307

(2005).

[27] J. M. Brown, E. A. Colbourn, J. K. G. Watson, and F. D. Wayne, J. Mol. Spectrosc. **46**, 37 (1973).

[28] H. Lefebvre-Brion and R. W. Field, *The Spectra and Dynamics of Diatomic Molecules* (Academic Press, New York, 2004).

[29] M. Mizushima, *The Theory of Rotating Diatomic Molecules* (John Wiley & Sons, New York, 1975).

[30] See EPAPS Document No. E-PLRAAN-75-206703 for the full data set of the experimental term values available for NaRb Ab complex. For more information ion EPAPS, see http://www.aip.org/pubservs/epaps.html.

[31] D. Stahel, M. Leoni, and K. Dressler, J. Chem. Phys. **79**, 2541 (1983).

[32] W. H. Press, S. A. Teukolsky, W. T. Vetterling, and B. P. Flannery, *Numerical Recipes in Fortran 77* (Cambridge University Press, Cambridge, England, 1999).

[33] I. Dabrowski, D. W. Tokaryk, and J. K. G. Watson, J. Mol. Spectrosc. **189**, 95 (1998).

[34] H. Kato, Bull. Chem. Soc. Jpn. **66**, 3203 (1993).

[35] E. R. Lippincott, J. Chem. Phys. **23**, 603 (1955).

[36] G. P. Barwood, P. Gill, and G. W. C. Rowley, Appl. Phys. B: Photophys. Laser Chem. **53**, 142 (1991).

[37] A. A. Surkus, R. J. Rakauskas, and A. B. Bolotin, Chem. Phys. Lett. **105**, 291 (1984).

[38] M. Gruebele, Mol. Phys. **69**, 475 (1990).

[39] M. Marinescu and H. R. Sadeghpour, Phys. Rev. A **59**, 390 (1999).

[40] I. Tuvi and Y. B. Band, J. Chem. Phys. **107**, 9079 (1997).

[41] D. G. Truhlar, J. Comp. Physiol. **10**, 123 (1972).

[42] R. B. Lenoucq, D. C. Sorensen, and C. Yang, *ARPACK User's Guide: Solution of Large Scale Eigenvalue Problems with Implicitly Restarted Arnoldi Methods* (1997), see http://www.caam.rice.edu/software/ARPACK/

[43] L. D. Landau and E. M. Lifshitz, *Qunatum Mechanics* (Pergamon, New York, 1965).

[44] F. Masnou-Seeuws and P. Pillet, Adv. At., Mol., Opt. Phys. **47**, 53 (2001).

[45] K. Willner, O. Dulieu, and F. Masnou-Seeuws, J. Chem. Phys. **120**, 548 (2004).

[46] T. Kiyoshima, S. Sato, E. A. Pazyuk, A. V. Stolyarov, and M. S. Child, J. Chem. Phys. **118**, 121 (2003).